minerals

MDPI

Article

Pyrophosphate-Inhibition of Apatite Formation Studied by In Situ X-Ray Diffraction

Casper Jon Steenberg Ibsen and Henrik Birkedal *

Department of Chemistry and iNANO, Aarhus University, Gustav Wieds Vej 14, 8000 Aarhus, Denmark; cjsibsen@hotmail.com

* Correspondence: hbirkedal@chem.au.dk; Tel.: +45-2250-8475

Received: 28 August 2017; Accepted: 12 February 2018; Published: 13 February 2018

Abstract: The pathways to crystals are still under debate, especially for materials relevant to biomineralization, such as calcium phosphate apatite known from bone and teeth. Pyrophosphate is widely used in biology to control apatite formation since it is a potent inhibitor of apatite crystallization. The impacts of pyrophosphate on apatite formation and crystallization kinetics are, however, not fully understood. Therefore, we studied apatite crystallization in water by synchrotron in situ X-ray diffraction. Crystallization was conducted from calcium chloride (0.2 M) and sodium phosphate (0.12 M) at pH 12 where hydrogen phosphate is the dominant phosphate species and at 60 °C to allow the synchrotron measurements to be conducted in a timely fashion. Following the formation of an initial amorphous phase, needle shaped crystals formed that had an octacalcium phosphate-like composition, but were too small to display the full 3D periodic structure of octacalcium phosphate. At later growth stages the crystals became apatitic, as revealed by changes in the lattice constant and calcium content. Pyrophosphate strongly inhibited nucleation of apatite and increased the onset of crystallization from minute to hour time scales. Pyrophosphate also reduced the rate of growth. Furthermore, when the pyrophosphate concentration exceeded ~1% of the calcium concentration, the resultant crystals had reduced size anisotropy suggesting that pyrophosphate interacts in a site-specific manner with the formation of apatite crystals.

Keywords: apatite; in situ X-ray diffraction; crystallization; nucleation; pyrophosphate; biomimetic materials

1. Introduction

The formation of nanocrystalline apatitic biomineral in the skeleton remains far from understood and, indeed, many open questions remain about apatite formation in general [1]. Apatite biomineralization occurs under strict biological control enforced by the collective action of numerous additives, including small molecules, such as citrate [2–5], pyrophosphate, and polyphosphates [6,7], as well as larger macromolecules. Pyrophosphate is involved in controlling apatite formation during skeleton formation and is a potent inhibitor of apatite crystallization [8–21]. In spite of the important roles of pyrophosphate as a mineralization inhibitor in vivo, no quantitative studies of its impact on nanocrystal formation kinetics have been performed to the best of our knowledge. Herein, we use in situ synchrotron powder diffraction [22–25] to quantify the impact of pyrophosphate on apatite formation from amorphous calcium phosphate (ACP).

We have previously shown that the shape and size of the formed apatite nanocrystals depend strongly on whether sodium or potassium salts are used as precursors [26], the pH of the starting solution, e.g., whether it is phosphate or hydrogenphosphate dominated [22,26], and the action of various additives [5,22,24,25,27,28]. Herein, we formed ACP from a sodium phosphate solution (pH ~12.3) and the resultant ACP phase is, therefore, hydrogen phosphate-rich. Apatite was formed

from hydrogen phosphate-rich ACP formed in situ by mixing a calcium chloride solution with a sodium phosphate solution to which various quantities of pyrophosphate were added according to:

$$10CaCl_2\ (aq) + 6\ Na_3PO_4\ (aq) + 10x\ Na_4P_2O_7\ (aq) \rightarrow ACP\ (s) \rightarrow apatite\ (s)$$

The counter ion determines the degree to which carbonate is incorporated into the lattice through co-substitution. In the case of potassium counter ion, carbonate incorporation into the lattice is reduced and we have previously shown that the apatite crystals obtained from such an ACP phase are long needles [22]. This was in contrast to the situation at higher pH (~12.5), at which the ACP phase is phosphate-dominated [26], where the crystals initially displayed almost spherical geometry and remained considerably less anisotropic, even at late stages of growth than the before mentioned long needles obtained at a slightly lower pH of 12.3. Therefore, the present work explores both the formation and morphology of apatite nanocrystals from hydrogen phosphate rich ACP with sodium as a counter ion and the impact of pyrophosphate additives thereon. In the case of potassium as a counter ion, we found, by a combination of diffraction and infrared spectroscopy, that the initial needle-shaped nanocrystals formed under the present pH conditions had octacalcium phosphate (OCP) stoichiometry, but without the 3D periodicity of OCP, because they were too thin [22].

2. Materials and Methods

We employed in situ X-ray diffraction [22–25,29,30] to follow the crystallization of apatite as in our previous work on other types of apatite formation [22,24,25]. We performed in situ synchrotron diffraction in a home built stopped flow apparatus with high temperature stability [24] by mixing equal volumes of a calcium chloride solution (0.4 M) with a sodium phosphate solution (0.24 M) loaded with varying quantities of sodium pyrophosphate (0–0.02 M). This gave a final calcium concentration in the mixture of 0.2 M, a total phosphate concentration of 0.12 M and a varying pyrophosphate concentration that we express as a percentage of the calcium concentration that thus varied from 0–5 mol% (i.e., concentrations of 0–0.01 M with the lowest pyrophosphate concentration being 1 mM). The pyrophosphate concentrations corresponded to 0.83–8.3 mol% of the phosphate concentration. This is higher than the values found in bone but approaches the values reported for resting cartilage ~0.7% [21,31]. The reactants were mixed by passing them through a liquid mixer and then directly into the reaction chamber (a single-crystal sapphire tube) where the reaction volume was investigated by synchrotron X-rays with a wavelength λ = 0.6829 Å at the Swiss Norwegian Beamlines at ESRF, Grenoble, France. Diffraction data were detected with a Dectris (CH) Pilatus 2 M detector placed at a sample-detector distance of 233.4 mm using 4 s exposure per data point. The present experiments were conducted at 60 °C. The 2D diffractograms were azimuthally integrated and corrected for beam-intensity fluctuations by normalizing the scattering intensity in the 1.12–1.44 $Å^{-1}$ q-range as in our previous work [22].

The results reported herein result from Rietveld refinement of diffraction data [27] that was conducted in GSAS [32]. The Rietveld model assumed a needle morphology of the crystallites (extensive testing of other morphologies indicated that this was an appropriate model) and incorporated refinement of lattice constants, calcium occupancy [22], scale factor, and a Chebyshev polynomial background.

3. Results

According to our previous studies, crystallization progressed via the initial formation of an amorphous phase [5,22,24,25,27], which was also confirmed by inspection of the raw diffraction data (not shown). The Rietveld refined scale factor is a direct measure of the amount of crystalline material and, thus, monitors the progress of crystallization. Figure 1 shows results from the pyrophosphate-free system and thus addresses the question of crystallization process for sodium as a counter ion. Qualitatively, the trends mirror those seen with potassium as counter ion [22], but the numerical values are different. Crystals formed after 6 min, as revealed by a rapid increase of the scale factor.

Before ~6 min, the scale factor fluctuated strongly (Figure 1A) due to a lack of, or extremely low, crystalline signals. After formation of the first crystals, the scale factor continued to increase, albeit at a slower rate, until ~25 min, after which it remained constant, indicating that the total amount of crystalline material did not change thereafter. The initial crystals were highly calcium-deficient as reflected by the refined calcium occupancy in Figure 1B. The calcium occupancy increased until ~20 min, after which it stabilized at 0.917(8) (the average value of the last 100 s of the experiment with the number in parentheses representing the root mean square deviation (RMSD) around the mean). At early stages, the lattice constants differed from the values at maturity, Figure 1E,F with the *a*- and *c*-axes being, respectively, smaller and larger than the late-stage values. The crystallite sizes also evolve with time, Figure 1C,D. When first formed, the crystals had an aspect ratio of about 7, but becomes less anisotropic during growth ending up with a final average crystal size of 6.2(2) × 30.5(6) nm (aspect ratio 4.9). The average crystallite size parallel to the *c*-axis drops somewhat over the 8 min following the initial crystal formation after which it is essentially constant. During this time, the scale factor increases, meaning that the amount of crystalline material, and by implication the number density of crystals, increases. Thus, the first detected crystals are very long, while later-forming crystals are shorter, resulting in a decrease in the average crystallite length. The rapid formation of high aspect ratio high-nonstoichiometric needles with deformed lattice constants is in agreement with the observations on the hydrogenphosphate-rich potassium system [22], but in contrast to the behavior at higher starting pH (~12.5) where the ACP is phosphate-dominated and the initial crystal have a low aspect ratio [26].

We previously [22] deduced a growth mechanism for the system with potassium as counter ion in which carbonate substitutions in the lattice do not play a role. The initial crystals were determined by a combination of diffraction and Fourier transform infrared (FTIR) spectroscopy data including time resolved measurements to be OCP-like, but without the 3D stacking order needed for real OCP crystals because the initially-formed crystals were so thin. During growth the crystals in average became increasingly apatitic to result in the constant calcium occupancy and lattice constants accompanied by the reduced crystallite size aspect ratio. A similar evolution of Ca-occupancy and crystal shape/size is seen in the present case (Figure 1D) showing that the same growth mechanism acts in the present sodium counter-ion case.

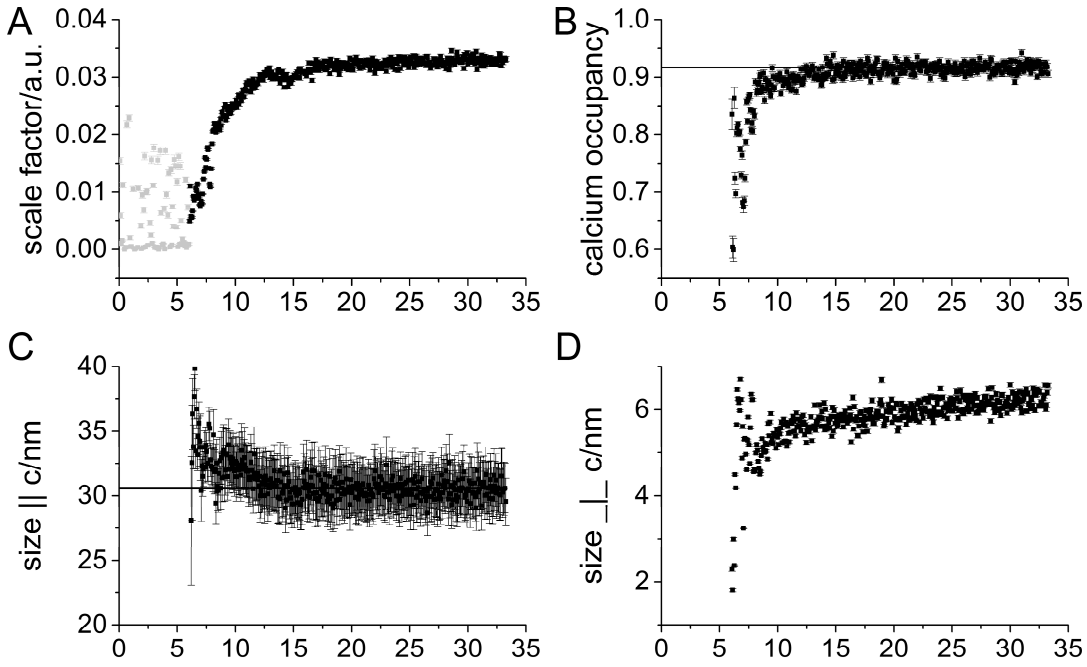

Figure 1. *Cont.*

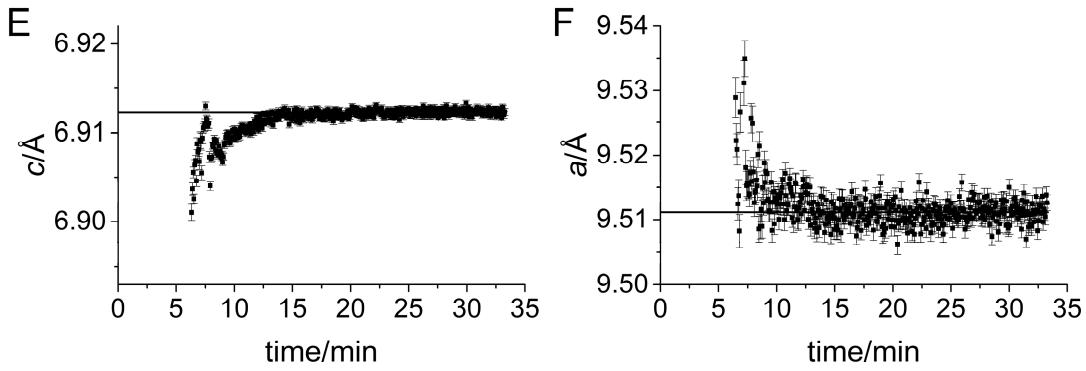

Figure 1. Results of Rietveld refinements of in situ diffraction data on the pyrophosphate free system. Horizontal lines represent the average of the last 100 s of the experiment. (**A**) Scale factor. Data points in gray are from refinements where the confidence in the results are lower due to convergence and/or local minima issues (see text); (**B**) refined calcium occupancy; (**C**,**D**) apparent crystallite sizes parallel and perpendicular to the *c*-axis, respectively; and (**E**,**F**) the refined lattice constants of the hexagonal apatite unit cell shown on the same relative scale. In panels (**B**–**F**), only results where the parameters were well-defined are shown; at earlier times the parameters were not determinable due to the extremely low or zero diffraction signal from apatite.

Impact of Pyrophosphate

Addition of pyrophosphate strongly impacted the crystallization kinetics. The results are summarized in Figures 2 and 3. Figure 2A compares the refined scale factors for different pyrophosphate concentrations with sigmoidal fits overlaid to further illustrate the trends. As evident from the data, pyrophosphate impacts both the time until first crystals are detected (nucleation time, Figure 2C), and the rate of transformation from amorphous to crystalline material, i.e., the slope of the curve (Figure 2B). The nucleation time was found to depend exponentially on pyrophosphate concentration, Figure 2C, featuring very significant stabilization of the ACP phase to the point of a retardation from minute to hour time scale. Results from repeated experiments are also shown to illustrate the excellent reproducibility of the data. This stabilization of ACP is in accordance with previous work by others at pH 8.5 measured ex situ [14]. The growth rate was likewise reduced as seen from the derivative of the scale factor time dependence, shown as the derivative of an analytical sigmoidal parameterization of the data in Figure 2B. In the presence of the additive, the crystallite size evolved qualitatively in the same manner as without additive, Figure 2D,E, i.e., with an aspect ratio that decreased with time. However, above a certain threshold concentration, in between 1.0% and 2.5% pyrophosphate, there was an abrupt change in the shape of the crystallites. The final length of the needles was reduced to 24.7(1) nm for all measured concentrations above 1.0%.

Concurrently, the size perpendicular to the long axis increased, to 9.0(1) nm, Figure 3A. This suggests that pyrophosphate binds specifically to specific crystal faces, probably the (002) surface inhibiting growth in this direction. Material was consequently redirected into thickening the crystallites, resulting in lowered aspect ratios (see Figure 3B). The fact that this behavior sets in above a threshold concentration suggests that the process is corporative and, thus, necessitates a critical pyrophosphate concentration to occur.

As in the pyrophosphate-free case, the calcium occupancy was also reduced during the initial growth stage when pyrophosphate was present indicating that the fundamental growth mechanism did not change, Figure 2I. With potassium as counter-ion, we previously deduced by in situ and ex situ diffraction, as well as time-resolved FTIR measurements that the crystals were hydrogen phosphate substituted with stoichiometries of the type $Ca_{10-x/2}(PO_4)_{6-x}(HPO_4)_x(OH)_2$ [22]. In the present case, the final calcium occupancy decreased with increasing pyrophosphate concentration, Figure 3D. Thus, the crystals become less stoichiometric when grown under the influence of pyrophosphate.

This is consistent with a scenario where a pyrophosphate substitute for two phosphates in the lattice structure (i.e., leaving also an anion vacancy). The resulting deficiency of negative charge could then conceivably be compensated by calcium vacancies resulting in stoichiometries of the type $Ca_{10-x/2-y}(PO_4)_{6-x-2y}(P_2O_7)_y(HPO_4)_x(OH)_2$ where additional carbonate substitutions have been left out. In this scenario, the lowest observed final calcium occupancy (for 5% pyrophosphate) of 0.86 in comparison the pyrophosphate-free value of 0.92 suggests that x ~1.6 and y ~0.7 so that the unit cell contains ~3.0 phosphates. This reflects the heavily disordered nature of these phases.

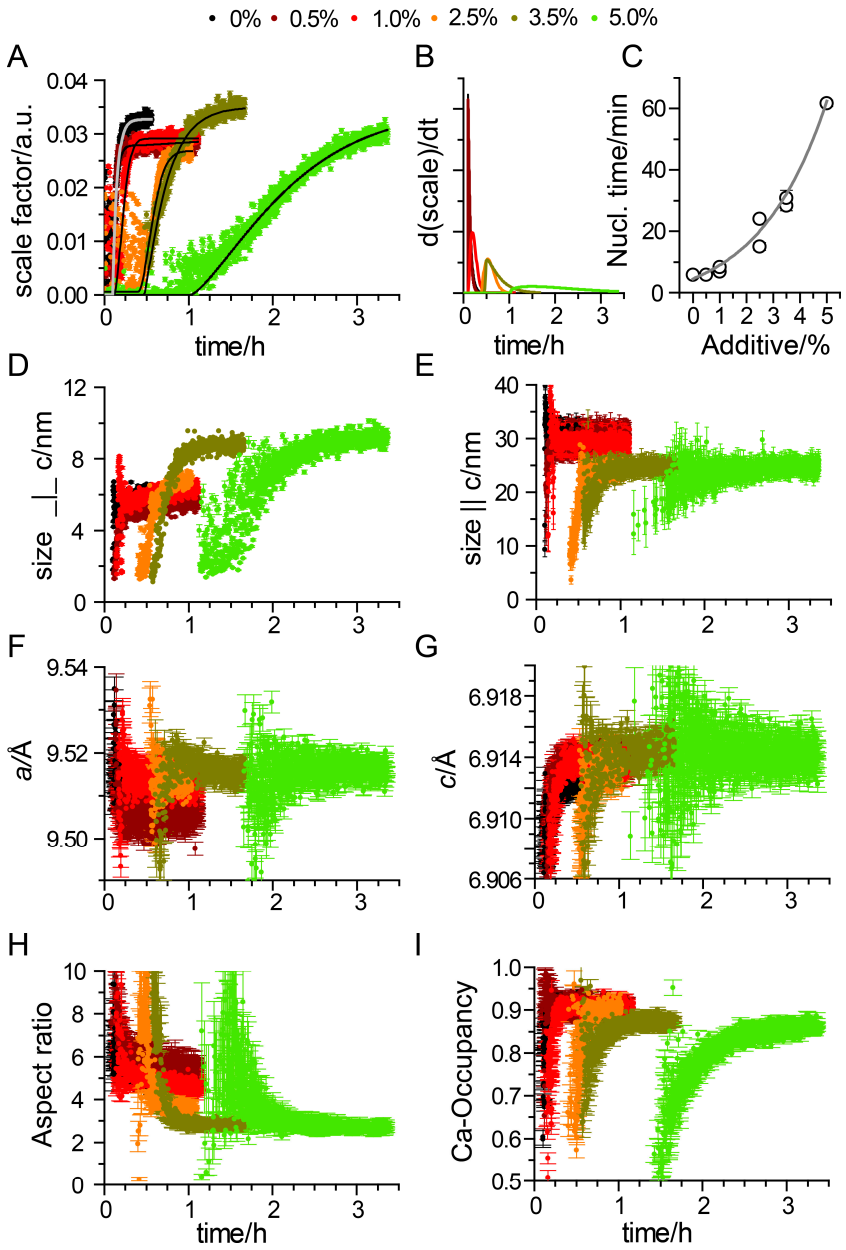

Figure 2. The impact of pyrophosphate on apatite formation kinetics derived from Rietveld refinements. The pyrophosphate concentration is given as molar percent of the calcium concentration. (**A**) The scale factor reflects the amount of crystalline material. The lines are sigmoidal fits to the data; (**B**) rate of growth in the amount of crystalline material as a function of time; (**C**) dependence of nucleation time on the amount of added additive; (**D**–**I**) time dependence of selected parameters; (**D**,**E**) crystallite sizes perpendicular and parallel to the *c*-axis, respectively; (**F**,**G**) apatite lattice constants; (**H**) crystallite size aspect ratio; and (**I**) calcium occupancy.

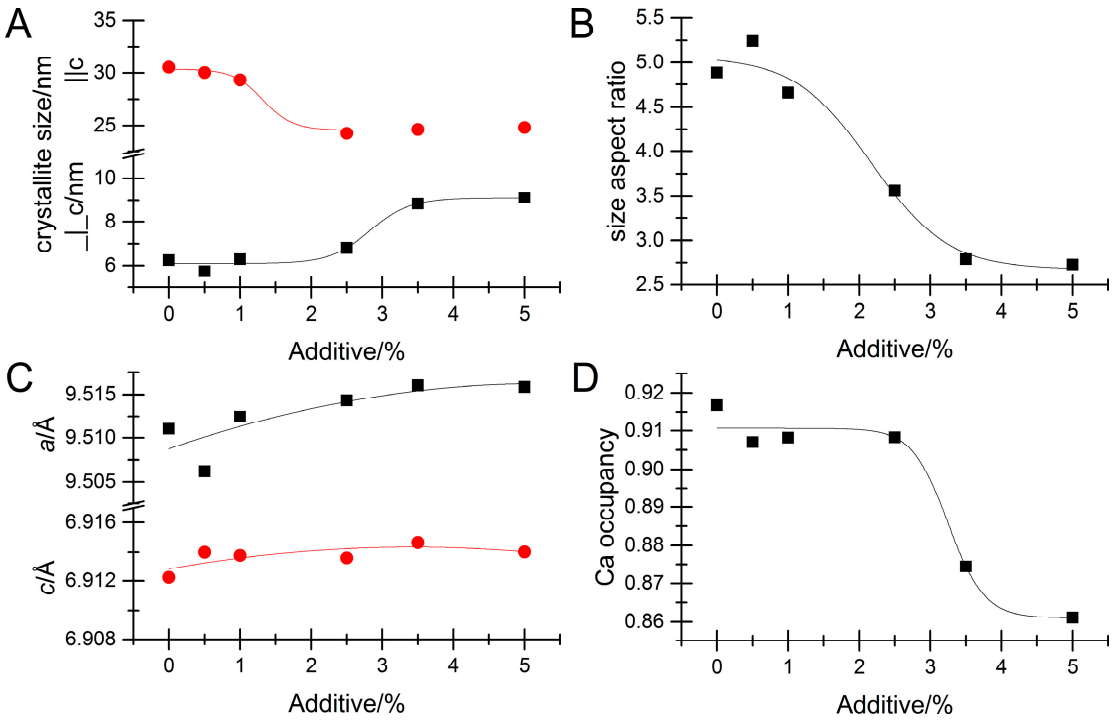

Figure 3. Values at long times of selected crystallographic parameters as a function of amount of added pyrophosphate. Lines are, in all cases, guides to the eye. The pyrophosphate concentration is given as a molar percent of the calcium concentration. (**A**) shows crystallite size along (red) and perpendicular (black to the *c*-axis); (**B**) shows the crystallite size aspect ratio (size$\|\|$**c**/size$\perp$**c**); (**C**) shows the lattice constants as a function of additive concentration while (**D**) gives the occupancy of the calcium sites in the apatite unit cell.

The lattice constants evolved in a manner similar to the additive free situation, but slowed down (see Figure 2F,G and Figure 3C). The final lattice constants do not display any significant dependency on pyrophosphate concentration indicating that only slight macrostrain is inflicted upon the crystals even though very specific interactions take place. This is in contrast to the impact of organic additives on $CaCO_3$ biominerals [33–37], ZnO [38,39], and apatite [25].

4. Discussion

The current use of in situ diffraction provided detailed information on the crystallization kinetics and behavior. We found, first of all, that the crystallization mechanism is akin to the one determined with potassium as a counter ion instead of sodium at the same pH [22]. Importantly, the initial crystallites did not attain the full 3D OCP structure because their thickness was of the same order as the stacking distance in OCP, which precludes the building of the 3D order and the telltale low-angle diffraction peak often used to detect OCP. The formation of an OCP-like intermediate was also found at a lower pH of 7.4 by Habraken et al. [40] suggesting that this pathway may be a general phenomenon in apatite formation when the solution pH is hydrogenphosphate dominated.

We further obtained insights into the inhibition of apatite formation due to pyrophosphate and found that pyrophosphate, as expected, strongly inhibits apatite crystallization and thereby increases the temporal stability of ACP. The fundamental mechanism of crystal formation via an initial OCP-like crystal was, however, unchanged, suggesting that this pathway may also occur in biogenic environments where additives abound.

Pyrophosphate additives resulted in nontrivial changes of crystal morphology above a threshold concentration suggesting a specific corporative interaction between pyrophosphate and the growing apatite nanocrystal.

Acknowledgments: We thank the Danish Agency for Science, Technology, and Innovation for funding (DANSCATT). The in situ diffraction experiments were performed on beamline BM01 (Swiss Norwegian Beam Lines) at the European Synchrotron Radiation Facility (ESRF), Grenoble, France. We are grateful to Dmitry Chernyshov at the ESRF for providing assistance in using beamline BM01. We further thank Vicki Nue for her assistance during the synchrotron experiments. Affiliation with the Center for Integrated Materials Research (iMAT) at Aarhus University is gratefully acknowledged.

Author Contributions: H.B. conceived the experiments. H.B. and C.J.S.I. designed the experiments, performed the experiments, and wrote the paper.

Conflicts of Interest: The authors declare no conflict of interest.

References

1. Birkedal, H. Phase transformations in calcium phosphate crystallization. In *New Perspectives on Mineral Nucleation and Growth: From Solution Precursors to Solid Materials*; Van Driessche, A.E.S., Kellermeier, M., Benning, L.G., Gebauer, D., Eds.; Springer International Publishing: Cham, Switzerland, 2017; pp. 199–210.
2. Davies, E.; Müller, K.H.; Wong, W.C.; Pickard, C.J.; Reid, D.G.; Skepper, J.N.; Duer, M.J. Citrate bridges between mineral platelets in bone. *Proc. Natl. Acad. Sci. USA* **2014**, *111*, E1354–E1363. [CrossRef] [PubMed]
3. Hu, Y.-Y.; Rawal, A.; Schmidt-Rohr, K. Strongly bound citrate stabilizes the apatite nanocrystals in bone. *Proc. Natl. Acad. Sci. USA* **2010**, *107*, 22425–22429. [CrossRef] [PubMed]
4. Reid, D.G.; Duer, M.J.; Jackson, G.E.; Murray, R.C.; Rodgers, A.L.; Shanahan, C.M. Citrate occurs widely in healthy and pathological apatitic biomineral: Mineralized articular cartilage, and intimal atherosclerotic plaque and apatitic kidney stones. *Calcif. Tissue Int.* **2013**, *93*, 253–260. [CrossRef] [PubMed]
5. Jensen, A.C.S.; Ibsen, C.J.S.; Birkedal, H. Transparent aggregates of nanocrystalline hydroxyapatite. *Cryst. Growth Des.* **2014**, *14*, 6343–6349. [CrossRef]
6. Omelon, S.; Georgiou, J.; Henneman, Z.J.; Wise, L.M.; Sukhu, B.; Hunt, T.; Wynnyckyj, C.; Holmyard, D.; Bielecki, R.; Grynpas, M.D. Control of vertebrate skeletal mineralization by polyphosphates. *PLoS ONE* **2009**, *4*, e5634. [CrossRef] [PubMed]
7. Omelon, S.; Grynpas, M.D. Relationships between polyphosphate chemistry, biochemistry and apatite biomineralization. *Chem. Rev.* **2008**, *108*, 4694–4715. [CrossRef] [PubMed]
8. Anderson, H.C.; Garimella, R.; Tague, S.E. The role of matrix vesicles in growth plate development and biomineralization. *Front. Biosci.* **2005**, *10*, 822–837. [CrossRef] [PubMed]
9. Anderson, H.C.; Shapiro, I.M. The epiphyseal growth plate. In *Bone and Development*; Bronner, F., Farach-Carson, M.C., Roach, H.I., Eds.; Springer: London, UK, 2010; pp. 39–64.
10. Anderson, H.C.; Sipe, J.B.; Hessle, L.; Dhamyamraju, R.; Atti, E.; Camacho, N.P.; Millán, J.L. Impaired calcification around matrix vesicles of growth plate and bone in alkaline phosphatase-deficient mice. *Am. J. Pathol.* **2004**, *164*, 841–847. [CrossRef]
11. Orriss, I.R.; Arnett, T.R.; Russell, R.G.G. Pyrophosphate: A key inhibitor of mineralisation. *Curr. Opin. Pharmacol.* **2016**, *28*, 57–68. [CrossRef] [PubMed]
12. Hessle, L.; Johnson, K.A.; Anderson, H.C.; Narisawa, S.; Sali, A.; Goding, J.W.; Terkeltaub, R.; Millán, J.L. Tissue-nonspecific alkaline phosphatase and plasma cell membrane glycoprotein-1 are central antagonistic regulators of bone mineralization. *Proc. Natl. Acad. Sci. USA* **2002**, *99*, 9445–9449. [CrossRef] [PubMed]
13. Fleisch, H.; Russell, R.G.G.; Straumann, F. Effect of pyrophosphate on hydroxyapatite and its implications in calcium homeostasis. *Nature* **1966**, *212*, 901–903. [CrossRef] [PubMed]
14. Fleisch, H.; Russell, R.G.G.; Bisaz, S.; Termine, J.D.; Posner, A.S. Influence of pyrophosphate on the transformation of amorphous to crystalline calcium phosphate. *Calcif. Tissue Res.* **1968**, *2*, 49–59. [CrossRef]
15. Fleisch, H.; Bisaz, S. Isolation from urine of pyrophosphate, a calcification inhibitor. *Am. J. Physiol. Leg. Content* **1962**, *203*, 671–675. [CrossRef] [PubMed]
16. Fleisch, H.; Straumann, F.; Schenk, R.; Bisaz, S.; Allgöwer, M. Effect of condensed phosphates on calcification of chick embryo femurs in tissue culture. *Am. J. Physiol.* **1966**, *211*, 821–825. [CrossRef] [PubMed]
17. Francis, M.D. The inhibition of calcium hydroxyapatite crystal growth by polyphosphonates and polyphosphates. *Calcif. Tissue Res.* **1969**, *3*, 151–162. [CrossRef] [PubMed]
18. Fleisch, H.; Neuman, W.F. Mechanisms of calcification: Role of collagen, polyphosphates, and phosphatase. *Am. J. Physiol.* **1961**, *200*, 1296–1300. [CrossRef] [PubMed]

19. Meyer, J.L.; McCall, J.T.; Smith, L.H. Inhibition of calcium phosphate crystallization by nucleoside phosphates. *Calcif. Tissue Res.* **1974**, *15*, 287–293. [CrossRef] [PubMed]
20. Meyer, J.L. Can biological calcification occur in the presence of pyrophosphate? *Arch. Biochem. Biophys.* **1984**, *231*, 1–8. [CrossRef]
21. Wuthier, R.E.; Bisaz, S.; Russell, R.G.G.; Fleisch, H. Relationship between pyrophosphate, amorphous calcium phosphate and other factors in the sequence of calcificationin vivo. *Calcif. Tissue Res.* **1972**, *10*, 198–206. [CrossRef] [PubMed]
22. Ibsen, C.J.S.; Chernyshov, D.; Birkedal, H. Apatite formation from amorphous calcium phosphate and mixed amorphous calcium phosphate/amorphous calcium carbonate. *Chem. Eur. J.* **2016**, *22*, 12347–12357. [CrossRef] [PubMed]
23. Jensen, A.C.S.; Hinge, M.; Birkedal, H. Calcite nucleation on the surface of PNIPAM-PAAc micelles studied by time resolved *in situ* PXRD. *Cryst. Eng. Commun.* **2015**, *17*, 6940–6946. [CrossRef]
24. Ibsen, C.J.S.; Birkedal, H. Influence of poly(acrylic acid) on apatite formation studied by in situ X-ray diffraction using an X-ray scattering reaction cell with high-precision temperature control. *J. Appl. Crystallogr.* **2012**, *45*, 976–981. [CrossRef]
25. Ibsen, C.J.S.; Birkedal, H. Modification of bone-like apatite nanoparticle size and growth kinetics by alizarin red S. *Nanoscale* **2010**, *2*, 2478–2486. [CrossRef] [PubMed]
26. Ibsen, C.J.S.; Leemreize, H.; Mikladal, B.F.; Skovgaard, J.; Eltzholtz, J.R.; Bremholm, M.; Iversen, B.B.; Birkedal, H. Crystallization kinetics of bone-like apatite nanocrystals formed from amorphous calcium phosphate in water by in situ synchrotron powder diffraction: Counter ions matter. 2018, in preparation.
27. Frølich, S.; Birkedal, H. Multiref: Software platform for automated and intelligent rietveld refinement of multiple powder diffractograms from in situ, scanning or diffraction tomography experiments. *J. Appl. Cryst.* **2015**, *48*, 2019–2025. [CrossRef]
28. Ibsen, C.J.S.; Gebauer, D.; Birkedal, H. Osteopontin strongly stabilizes metastable states prior to nucleation during apatite formation. *Chem. Mater.* **2016**, *28*, 8550–8555. [CrossRef]
29. Olliges-Stadler, I.; Rossell, M.D.; Suess, M.J.; Ludi, B.; Bunk, O.; Pedersen, J.S.; Birkedal, H.; Niederberger, M. A comprehensive study of the crystallization mechanism involved in the nonaqueous formation of tungstite. *Nanoscale* **2013**, *5*, 8517–8525. [CrossRef] [PubMed]
30. Jensen, G.V.; Bremholm, M.; Lock, N.; Deen, G.R.; Jensen, T.R.; Iversen, B.B.; Niederberger, M.; Pedersen, J.S.; Birkedal, H. Anisotropic crystal growth kinetics of anatase TiO_2 nanoparticles synthesized in a nonaqueous medium. *Chem. Mater.* **2010**, *22*, 6044–6055. [CrossRef]
31. Bisaz, S.; Russell, R.G.G.; Fleisch, H. Isolation of inorganic pyrophosphate from bovine and human teeth. *Arch. Oral Biol.* **1968**, *13*, 683–696. [CrossRef]
32. Larson, A.C.; Von Dreele, R.B. *Los Alamos National Laboratory Report Laur 86-748*; Los Alamos National Laboratory: Los Alamos, NM, USA, 2000.
33. Leemreize, H.; Eltzholtz, J.R.; Birkedal, H. Lattice macro and microstrain fluctuations in the calcified byssus of Anomia simplex. *Eur. J. Miner.* **2014**, *26*, 517–522.
34. Frølich, S.; Sørensen, H.O.; Hakim, S.S.; Marin, F.; Stipp, S.L.S.; Birkedal, H. Smaller calcite lattice deformation caused by occluded organic material in coccoliths than in mollusk shell. *Cryst. Growth Des.* **2015**, *15*, 2761–2767. [CrossRef]
35. Pokroy, B.; Fitch, A.N.; Lee, P.L.; Quintana, J.P.; Caspi, E.N.; Zolotoyabko, E. Anisotropic lattice distortions in mollusk-made aragonite: A widespread phenomenon. *J. Struct. Biol.* **2006**, *153*, 145–150. [CrossRef] [PubMed]
36. Pokroy, B.; Fitch, A.N.; Marin, F.; Kapon, M.; Adir, N.; Zolotoyabko, E. Anisotropic lattice distortions in biogenic calcite induced by intra-crystalline organic moleucles. *J. Struct. Biol.* **2006**, *155*, 96–103. [CrossRef] [PubMed]
37. Pokroy, B.; Quintana, J.P.; Caspi, E.N.; Berner, A.; Zolotoyabko, E. Anisotropic lattice distortions in biogenic aragonite. *Nat. Mater.* **2004**, *3*, 900–902. [CrossRef] [PubMed]
38. Brif, A.; Ankonina, G.; Drathen, C.; Pokroy, B. Bio-inspired band gap engineering of zinc oxide by intracrystalline incorporation of amino acids. *Adv. Mater.* **2014**, *26*, 477–481. [CrossRef] [PubMed]

39. Brif, A.; Bloch, L.; Pokroy, B. Bio-inspired engineering of a zinc oxide/amino acid composite: Synchrotron microstructure study. *Cryst. Eng. Comm.* **2014**, *16*, 3268–3273. [CrossRef]
40. Habraken, W.J.E.M.; Tao, J.; Brylka, L.J.; Friedrich, H.; Bertinetti, L.; Schenk, A.S.; Verch, A.; Dmitrovic, V.; Bomans, P.H.H.; Frederik, P.M.; et al. Ion-association complexes unite classical and non-classical theories for the biomimetic nucleation of calcium phosphate. *Nat. Comm.* **2013**, *4*, 1507. [CrossRef] [PubMed]